Photo- and Electroluminescence from Zn-Doped InN Semiconductor Nanocrystals

Simon M. Fairclough, Peter N. Taylor, Charles T. Smith, Pip C. J. Clark, Stefan Skalsky, Ruben Ahumada-Lazo, Edward A. Lewis, Daniel J. Tate, Ben F. Spencer, Mary Burkitt-Gray, Igor Píš, Federica Bondino, Patrick Bergstrom-Mann, Sadie Carter-Searjeant, Michael L. Turner, David Binks, Sarah J. Haigh, Wendy R. Flavell, Richard J. Curry,* and Mark A. Green*

There is a critical research need for efficient luminescent colloidal nanocrystals, free from cadmium and lead whose toxicity subjects them to usage restrictions, with applications from display devices to biology. Approaches to directly replace cadmium-based materials have mainly focused on indium phosphide-based nanocrystals, however these too are subject to concerns over toxicity. Few other alternatives have been found that can compete with the emission range and efficiency of Cd- and Pb-based nanocrystals. Group III-nitride nanocrystals, and their alloys, offer the exciting potential to tune bandgap energies from the ultraviolet to the near infrared yet a robust route toward efficient luminescent nitride nanocrystals is lacking. Here, the synthesis of photoluminescent indium zinc nitride quantum dots exhibiting tunable emission through the visible to near infrared spectra region, with quantum yields of up to 30% is reported. Capping the nanocrystals with both a GaN and ZnS shell significantly increases air stability and emission quantum yields. A proof-of-principle indium zinc nitride nanocrystal light emitting diode is also demonstrated. This work overcomes the significant challenges that have prevented the full exploration of nitride-based semiconductor nanocrystal development, providing a new system for further exploration as a heavy-metal free alternative to current state-of-the-art materials.

1. Introduction

The development of colloidal semiconductor nanocrystals (NCs) has provided a new generation of high-efficiency luminescent materials whose emission wavelength is tunable across the visible and near infrared (IR) spectral region.[1] The ability to chemically engineer their structure and incorporate them within other organic and inorganic hosts has led to their widespread demonstration as optically active materials in a variety of devices from photonics,[2] through to biological sensing.[3] However, these materials have, to date, suffered from concerns relating to the toxic nature of the heavy metal elements (such as Cd and Pb) that are typically present in the NC core of the best performing materials. There is therefore significant effort to develop alternative NC material systems that, while providing the same functionality as existing NC systems (e.g., CdSe and PbS), do not rely upon

Dr. S. M. Fairclough, Dr. M. Burkitt-Gray, Dr. P. Bergstrom-Mann,
S. Carter-Searjeant, Prof. M. A. Green
Department of Physics
King's College London
Strand, London WC2R 2LS, UK
E-mail: mark.a.green@kcl.ac.uk

Dr. P. N. Taylor
Sharp Life Science (EU) Ltd.
The Hayakawa Building, Edmund Halley Road, Oxford Science Park,
Oxford OX4 4GB, UK

Dr. C. T. Smith, Prof. R. J. Curry
Department of Electrical and Electronic Engineering
Photon Science Institute
The University of Manchester
Oxford Road, Manchester M13 9PL, UK
E-mail: richard.curry@manchester.ac.uk

The ORCID identification number(s) for the author(s) of this article can be found under https://doi.org/10.1002/adom.202000604.

Dr. P. C. J. Clark, Dr. S. Skalsky, Dr. R. Ahumada-Lazo, Dr. D. Binks,
Prof. W. R. Flavell
Department of Physics and Astronomy
Photon Science Institute
The University of Manchester
Oxford Road, Manchester M13 9PL, UK

Dr. E. A. Lewis, Dr. B. F. Spencer, Prof. S. J. Haigh
Department of Materials
The University of Manchester
Oxford Road, Manchester M13 9PL, UK

Dr. D. J. Tate, Prof. M. L. Turner
Department of Chemistry
The University of Manchester
Oxford Road, Manchester M13 9PL, UK

Dr. I. Píš
Elettra-Sincrotrone Trieste S.C.p.A.
S.S. 14 km 163.5 in AREA Science Park, Basovizza, Trieste 34149, Italy

Dr. F. Bondino
IOM CNR
Laboratorio TASC, S.S. 14 km 163.5 in AREA Science Park, Basovizza,
Trieste 34149, Italy

heavy metal constituents. Once achieved it is anticipated that NC usage will increase as regulatory barriers preventing the use of Cd- and Pb-based materials are circumvented thus enabling the impact of NC-based technologies to be significantly extended.

Group III-nitride semiconductors offer the possibility to tune their intrinsic band gap energy from the IR through to the ultraviolet (UV) using a combination of alloying and quantum confinement effects. To date, nitride-based systems have been mainly realized via chemical vapor deposition and molecular beam epitaxy routes,[4] to produce an array of nitride structures.[5] Of these, InGaN has been most notable, providing efficient blue light-emitting diodes (LEDs) and laser diodes among other optoelectronic applications.[6] Significantly, colloidal chemistry routes to nitride NCs have not been forthcoming.[4a,5,6,7] Achieving this is of great importance as they may fulfil the urgent need for size-tunable non-toxic alternatives to existing NCs, as active regions for photovoltaic and LED applications, and as fluorophores for biomedical imaging.[8] The few existing examples of nitride nanoparticle production mainly utilize non-colloidal methods due to the lack of a safe synthesis route, requiring significant subsequent effort to render them solution processable,[5,7,9] and have shown no significant photoluminescence (PL).[9a,b] The colloidal synthesis of nitride nanoparticles has only very recently been reported,[9b,d,10] and only in the case of Zn_3N_2 and GaN shown PL.[9d,10b,c] The resulting nanoparticles however can suffer from oxidation or surface oxidation upon exposure to oxygen, potentially leading to difficulties in their application.[9d,10b] While indium nitride has recently been synthesized via a sodium amide ($NaNH_2$) method, no PL was observed due to the high free carrier density relating to the observation of surface plasmons.[9a,b,10a] It is known within InX (X = P, As) and GaN nanoparticle systems, and epitaxial nitrides, that the introduction of zinc during synthesis leads to emission.[10b,11] Within epitaxially grown nitrides, Zn doping enhances emission through either p-type doping or through other defect behavior,[12] while the origins of the PL enhancement within Zn doped III-V nanoparticles systems remains unclear and is the focus of much research.[10b,11] Here we apply this approach to demonstrate the non-volatile synthesis and characterization of indium zinc nitride-based NCs ($InZn_xN$) that exhibit strong tunable PL across the visible and near IR spectrum. We further demonstrate the ability to form core-shell structures to further stabilize the NCs and thereby open up a route to realizing colloidal nitride NC technologies and provide a demonstration of quantum dot light emitting device (QDLED).

2. Results and Discussion

The synthesis is based on the reaction of metal salts (indium iodide and zinc stearate or zinc oleate) with $NaNH_2$ as described in the Experimental Section. An excess of nitrogen precursor (at an elemental ratio of In:Zn:N of 1:1:21) was utilized through a 'heat up' technique to a growth temperature of 240 °C. Luminescent InZnN NCs were synthesized with an onset of absorption at ≈450 nm after 1 min of growth, subsequently red shifting to ≈650 nm after a total of 40 min (**Figure 1**a). The
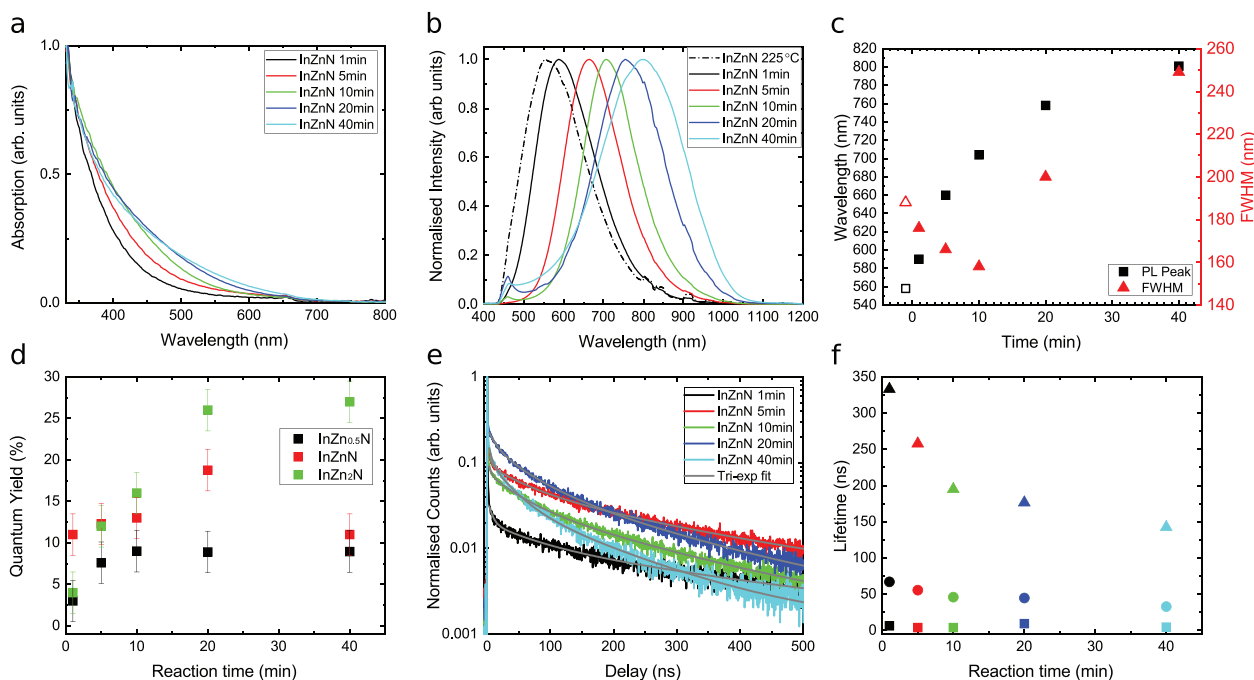

Figure 1. a) Absorption spectra and b) photoluminescence spectra of nanocrystals synthesized with 1:1 In:Zn precursor stoichiometry at a reaction temperature of 240 °C. Included in (b) is data from an aliquot taken at 225 °C to show the onset of photoluminescence during the heat up process (dot-dashed line). c) The evolution of the photoluminescence peak (black squares) and FWHM (red triangles) with reaction time. For comparison the 225 °C aliquot is also included (open symbols). d) Photoluminescence quantum yields values for the nanocrystals synthesized as a function of In:Zn precursor ratio and reaction time. e) Photoluminescence lifetime decay transients measured as a function of reaction time with corresponding lifetimes obtained from f) tri-exponential fitting shown (square, circle, and triangle are τ_1, τ_2, and τ_3, respectively).

absorption edge did not exhibit any excitonic features, although photoluminescence excitation (PLE) spectra displayed features consistent with excitonic behavior (Figure S1, Supporting Information). The NCs exhibited bright PL at ≈590 nm after 1 min of growth, red shifting to ≈800 nm after 40 min (Figure 1b). The PL full width at half maximum (FWHM) was initially broad, starting at ≈190 nm and gradually narrowing to ≈160 nm after 10 min growth (Figure 1c), indicative of size 'focusing' growth during this initial period (vide infra).[13] The PL FWHM then increased to ≈250 nm as the growth continued for up to 40 min. The PL quantum yields (QY) of the NCs were measured to be ≈10% after 1 min of growth, reaching a maximum of 18% after 20 min growth, with a PL maximum of 750 nm (Figure 1d). After a total of 40 min growth, the QY was found to have reduced to ≈12%. The observation of an optimum QY as function of NC reaction time, also known as a 'bright point', has been previously attributed to an optimally reconstructed surface or crystal reconstruction.[14] While the growth temperature was set at 240 °C, aliquots taken upon heating of the reaction solution showed that PL could also be observed at temperatures as low as 225 °C but with a low QY.

Varying the In:Zn precursor ratio from 1:1 resulted in materials with broadly similar spectral profiles, although the emission range obtained was modified. Using an In:Zn ratio of 2:1 ($InZn_{0.5}N$) and a reaction temperature of 240 °C over a 40 min growth, a NC PL maximum ranging from ≈600 to ≈700 nm (Figure S2a, Supporting Information) was observed. Similar spectra were also obtained for a In:Zn ratios of 1:1 (InZnN) and 1:2 ($InZn_2N$) (Figure S2b,c Supporting Information), with the later for example displaying PL onset at 590 nm and following 40 min growth a red shifted PL maximum at ≈730 nm. This is between that obtained from the corresponding $InZn_{0.5}N$ and InZnN samples (665 and 800 nm, respectively). This is clearly evidenced by the images of the NC samples excited using a UV lamp, displaying green to red tuning of emission with reaction time (Figure S2, Supporting Information), and further seen to emit into the near IR using a near IR camera. In all cases, the PL FWHM varied between 160 and 240 nm, reducing over the initial 10 min of NC growth prior to subsequent broadening as the growth continued (Figure S2, Supporting Information).

The most notable effect of varying the precursor ratio was the increase in PL QY with increasing Zn content. PL QYs of 28% were obtained from $InZn_2N$ NCs, reducing to 18% and 9% for InZnN and $InZn_{0.5}N$, respectively (Figure 1d). This highlights the importance of the incorporation of Zn into the materials as a means of obtaining efficient PL.

The PL lifetimes, shown in Figure 1e,f and Figure S3, Supporting Information, exhibit tri-exponential decay behavior (the rapid initial drop in each case is attributed to scattering of the excitation beam, which is not resolvable on the measurement time-scale and so was omitted from the fitting.). This tri-exponential behavior showed only small variations in lifetime when spectrally resolved over the PL emission, indicating consistent recombination dynamics within the ensemble of emitting NCs (Figure S1, Supporting Information). A dominant longer lifetime component (≈350–150 ns) displayed a dependence on reaction time and composition (Figure 1f; Figure S3, Supporting Information) and is discussed below. Shorter, less dominant PL decay lifetimes were found with a fast component of ≈5 ns and a second component in the region of 25–65 ns. These PL lifetimes are the same order of magnitude as GaN and Zn_3N_2 nanocrystals made by other methods.[10b,15]

Cyclic voltammetry was utilized to obtain the NC electronic band alignments. **Figure 2**a shows the onset of reduction and oxidation occurring at −0.3 ± 0.1 V and 1.3 ± 0.1 V for InZnN, and at −0.5 ± 0.1 V and 1.4 ± 0.1 V for $InZn_2N$ versus Ag/AgNO₃. Calibration to ferrocene provided valence and conduction band energies of −6.7 ± 0.1 and −4.9 ± 0.1 eV, and −6.7 ± 0.1 and −4.8 ± 0.1 eV, relative to vacuum for InZnN and $InZn_2N$, respectively (Figure 2b). These values correlate to that of InN NCs made without the Zn precursor (−6.5 ± 0.1 and −4.9 ± 0.1 eV) which shows quantum confinement, and the InN band alignments known from experiment and literature,[16] which have no quantum confinement (Figure 2b). This indicates a prevalence toward a Zn-doped InN based structure in these nanocrystals rather than In-doped Zn_3N_2 or a mixing of the electronic structures.[12c,16,17]

Electron microscopy of the samples prepared using differing precursor ratios confirmed the presence of nanocrystalline material (**Figure 3**; Figures S4–S6, Supporting Information).
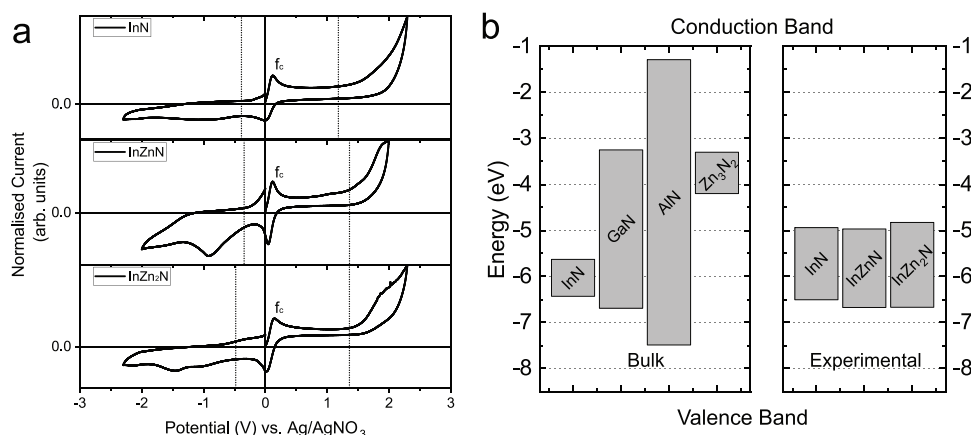

Figure 2. a) Cyclic voltammograms (CV) of InN, InZnN, and $InZn_2N$ nanocrystals with a ferrocene reference (f_c), for clarity the dotted lines relate to points of oxidation and reduction. b) Literature bulk band alignments relative to vacuum for InN, GaN, AlN,[16] and Zn_3N_2,[17] compared to experimental determined band alignments as calculated from the nanocrystal CV of (a).

**ADVANCED
SCIENCE NEWS**

www.advancedsciencenews.com

**ADVANCED
OPTICAL
MATERIALS**
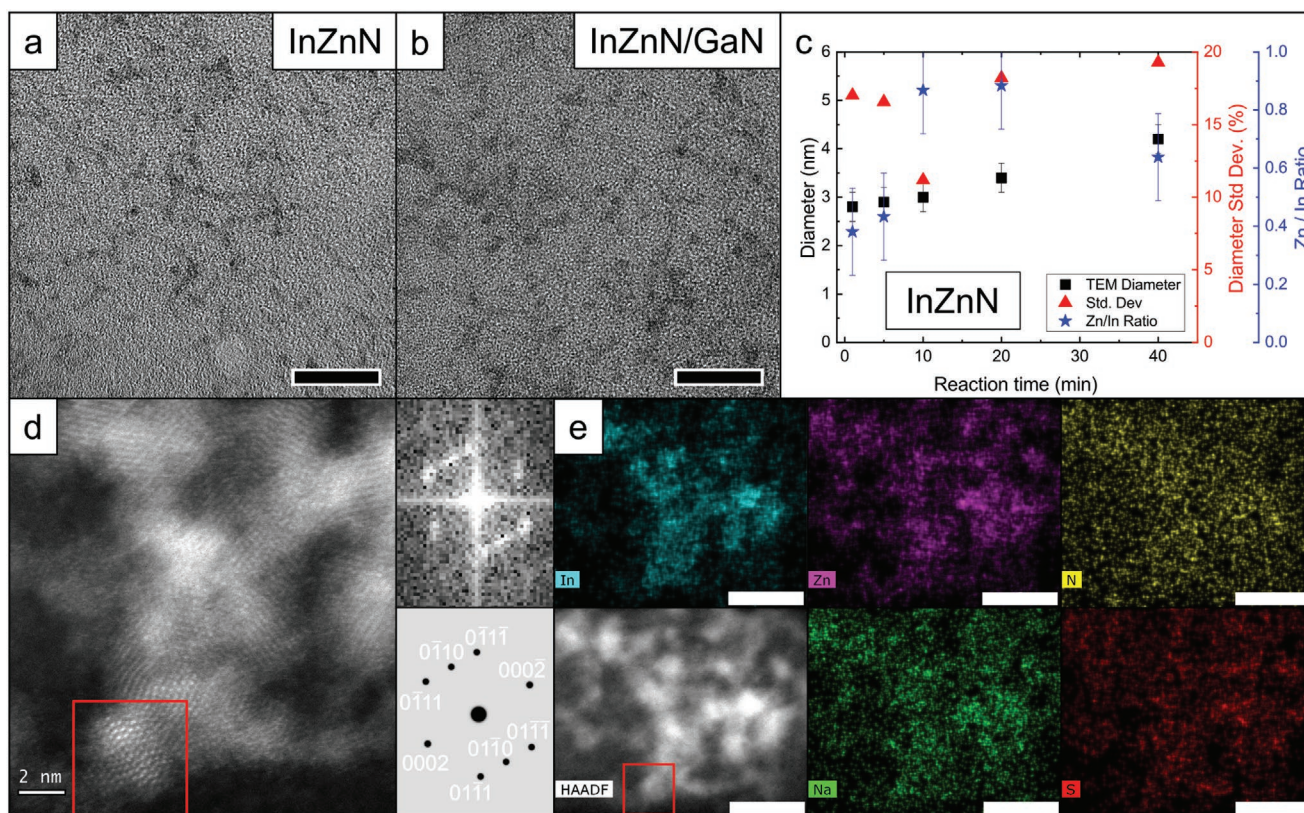
www.advopticalmat.de

Figure 3. TEM images of a) InZnN after 40 min of growth, scale bar 20 nm, and b) InZnN with 1 monolayer of GaN, scale bar 20 nm. c) The corresponding mean nanocrystal diameter (squares), diameter standard deviation (triangles), and Zn/In ratio (stars) as determined by TEM and EDS, respectively, as a function of reaction time. d) A high-resolution HAADF-STEM micrograph of a cluster of InZnN NCs of (a) with the upper right insert corresponding to Fourier transform of the highlighted red region, scale bar 2 nm. The lower right inset is the corresponding simulated diffraction pattern for hexagonal InN oriented in the [100] closely matching the experimental pattern. e) Shows the STEM-EDS elemental maps showing In (Cyan), Zn (Magenta), N (Yellow), Na (Green), and S (Red), all scale bars 10 nm.

Materials prepared with a precursor ratio of InZnN exhibited NCs with a spherical-like morphology and a tendency to aggregate due to the amount of cleaning required (up to 5 cycles), consistent with other III–V-based colloidal NCs, exhibiting diameters ranging from 2.8 to 5.1 nm from 1 to 40 min growth, with standard deviations of between 12% and 20% (Figure 3c). Initial growth (up to a reaction time of 10 min) showed a focusing of the size distribution, thereafter a size broadening occurred correlating with the reduction and then broadening of the PL FWHM, respectively seen in Figure 1c. This confirmed that the large PL FWHM was dominated by inhomogeneous broadening.

Energy dispersive spectroscopy (EDS) characterization of the InZnN NCs as a function of reaction time was undertaken. The results indicate that the Zn:In ratio within the NCs varies with reaction time, Figure 3c, offering the potential for different reaction and doping dynamics to be utilized as demonstrated in other systems.[18] The NCs presented an In-rich seed after 1 min of growth, coinciding with a low PL QY (Figure 1d and Figure 3c). Following a further ≈10–20 min period of growth, the increase in NC diameter coincided with an increase in Zn content to a In:Zn ratio of close to 1:1, and resulted in the highest PL QY for these nanocrystals. Continued growth for up to 40 min total reaction time resulted in a decrease in Zn

content, highlighting the complexity of the NC synthesis reaction. This aligns with theoretical predictions and experimental investigation of Zn-doped InN thin films, showing that incorporation of Zn is energetically unfavorable at InN surfaces,[12c,19] and suggests the potential for Na incorporation for long reaction times within this system.

High resolution scanning transmission electron microscopy (STEM) and powder X-ray diffraction (XRD) showed these materials to be nanocrystalline, displaying the main reflection (100), (002), and (101) reflections of hexagonal crystal structure seen in Figure 3d, Figures S5,S6, Supporting Information. The d-spacing and lattice plane orientations follow similarly to that of hexagonal InN structure, albeit slightly strained (Figure S5, Supporting Information),[20] and are not the anti-bixbyite structure of bulk Zn_3N_2,[21] which would have suggested the formation of an In doped Zn_3N_2 structure. This was further supported by STEM-EDS (Figure 3e) highlighting the co-localization of Zn to In consistent with a Zn-doped InN alloy. It is known that within Zn-doped InN thin films, a wide array of alloying and defect/strain effects can influence these reflections, which could account for the complex crystal structures which is discussed further in the Supporting Information.[12c] It must be noted that upon a few minutes of exposure to air, the uncapped NCs were found to oxidize, as seen by other

ADVANCED
Science News

www.advancedsciencenews.com

ADVANCED
OPTICAL
MATERIALS

www.advopticalmat.de

nitride systems, and demonstrated by XRD (Figures S7,S8, Supporting Information) resulting in a shift in XRD reflections, which could not be unequivocally assigned to a single phase of a different known material. Comparison of reflections following oxidation with predicted diffraction patterns of the known phases of InN, Zn_3N_2 ZnO, In_2O_3 showed no conclusive evidence of a new product (Figures S7,S8, Supporting Information). Low fraction oxygen indium oxynitride (InO_xN) and zinc oxynitride (ZnO_xN), exhibit similar diffraction patterns (dependent of oxygen composition) and serve as the most probable candidate.[22]

X-ray photoelectron spectroscopy (XPS) showed In, Zn, and N as expected from an InZnN doped material, closely following the In:Zn ratio determined by EDS although the N content of the NCs determined by EDS was consistently lower than that given by XPS (Table S1 and Figures S9–S12, Supporting Information). Investigations have shown that this could be attributed to electron beam damage, consistent with a significantly higher Mott cross-section of N anions than that of In cations for high acceleration voltages (greater than 200 kV).[23] This was further supported by the observed degradation (melting) of the NC structure under an 300 kV electron beam exposure (Figure S13, Supporting Information).[9d,23] Observing the NCs at lower magnification and at lower acceleration voltage (80 kV) has been shown to improve stability.

Synchrotron radiation X-ray photoelectron spectroscopy (SR-XPS) was used to depth-profile the stoichiometry of the NC non-destructively. Tuning the synchrotron X-rays and utilizing the known inelastic mean free path of specific photoionization electron binding energies at fixed kinetic energies (KE) and correcting for known X-ray cross sections allowed the stoichiometry to be determined for given sampling depths. Low KE (225 eV) were estimated to have mean sampling depth of 2.0 nm, while increasing the KE to 550 and 800 eV increased the sampling depth to ≈3.5 and 4.6 nm, respectively. Table S2 and Figures S9,S10, Supporting Information, show that the NCs were homogenously doped materials, within the error of the technique, with little variation in In:Zn:N ratio with sample depth, and showed an In:Zn ratio consistent with EDS. The In $3d_{5/2}$ peak at 445.0 eV ± 0.1 eV and N 1s at 398.8 eV ± 0.1 eV binding energies, as determined by SR-XPS were consistent with those of characteristic InN and similar structures.[24] Further species were observed for the N 1s and In $3d_{5/2}$ core levels at the lowest sampling depth (225 eV, Figures S11 and S12, respectively, Supporting Information). The N 1s peak at 400.4 eV ± 0.1 eV could be attributed to protonated N species, such as amines and ammonia, and the higher binding energy the In 3d peaks was consistent with In hydroxide or In oxynitride.[22,25] These species are well-known decomposition products for nitrides upon exposure to moisture or oxygen respectively.[26] Sulfur was also found predominantly at the surface, with an S $2p_{3/2}$ binding energy of 162.1 eV ± 0.1 eV indicative of a bound thiol species suggesting that hexadecanethiol is still present as the ligand.[27] This was also supported by our use of alternative ligands to thiols, such as a phosphines and amines, which showed similar peak PL emission but significantly lower QY.

Interestingly, Na from the $NaNH_2$, though not to be involved in the initial growth and not seen in any previous reported reactions,[9a,10] was also found to be incorporated into the NC structure for the longest reactions. This is supported by negligible subsurface Na being observed for short reactions (Table S2, Supporting Information) while for the longest reactions, its presence was observed. It is suggested that the element could be substituting Zn sites through diffusion-based cationic exchange or occupying interstitial sites as a half-Heusler compound (such as NaZnN) shell species, which have been theoretically predicted but not currently fully realized.[28] This Na incorporation can also explain the reduction in PL lifetime seen in Figure 1e and most prominently in Figure S3c, Supporting Information, but also via passivation of trap sites within the NCs and thereby reducing the long component of the PL lifetime. These results lead to a current understanding of the NC reaction and structure, as suggested in Figure S14, Supporting Information, in which an In-rich seed is initially formed followed by NC growth and Zn diffusion. As the reaction proceeded to longer times, full decomposition of $NaNH_2$ occurs allowing Na to diffuse into the NC, passivating traps while also potentially making a half-Heusler compound at the surface.

To reduce the NC sensitivity to oxidation, a simple shelling procedure utilizing zinc diethyldithiocarbamate was performed to produce InZnN/ZnS core/shell NCs. The addition of a ZnS shell, while not fully optimized, resulted in a monolayer of growth, a small shift in PL (**Figure 4**a), and an increase of QY from 18% to 21%. This was accompanied by an increase in the PL lifetimes from 126 to 142 ns (Figure 4b,c) showing that ZnS shelling passivated non-radiative recombination sites of the core particles. The ZnS shell was found to extend the stability of NC PL, when exposed to air, from tens of minutes to several hours (Figure 4d). An increase of PL intensity of 10% was seen for the ZnS shelled nanocrystals (Figure 4d), highlighting a photo brightening stage, as seen with other air-exposed nanoparticle materials.[29] The PL stabilized after 3 h exposure and PL could be seen for several days. Enhanced structural stability following shelling was also seen under the electron beam, for example, the stoichiometry of constituent elements was found (by EDS) to be $In_{1.0}Zn_{0.7}N_{0.3}$ for a InZnN core-only structure (Table S3, Supporting Information), while for InZnN/ZnS values of $In_{1.0}Zn_{0.7}N_{1.8}/Zn_{1.1}S_{1.5}$ were measured, assuming a constant core In:Zn stoichiometry before and after shelling. Similarly, a monolayer of GaN was also added to InZnN nanocrystals (Figure 3b) which increased the PL QY from 18% to 25%. The photostability of InZnN/GaN was an improvement on the core-only structure, but photobleached over a 12-h period (Figure 4d). A further monolayer of ZnS on the InZnN/GaN nanocrystals increased the PL QY from 25% to 29%, a significant increase from the core only nanoparticle (core 18%), and stabilized the nanocrystals for several days highlighting the importance of shelling. Throughout the shelling studies, only minor variations of PL lifetimes were observed (Figure 4c), consistent with values expected from a type-I heterostructure (Figure 2b). While we currently assign this structure as a doped-nitride and suggest the emission is band edge in origin, it is well known that defects and dopants play a large role in the emission of nitrides and III-V materials in general.[24b,30] It must be noted that the complexities of the material and reaction could mask the effects of defects and potential dopants,
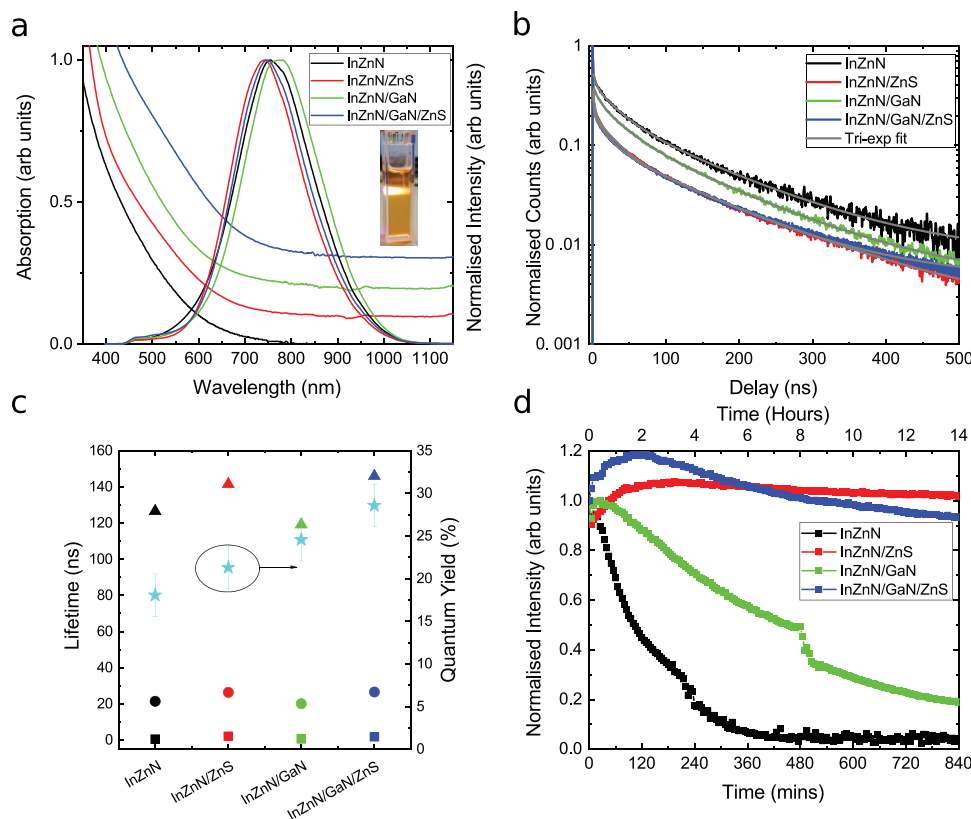
Figure 4. a) Characteristic absorption and photoluminescence spectra of InZnN, InZnN/ZnS, InZnN/GaN, and InZnN/GaN/ZnS nanocrystals. Inset to (a) is an image of InZnN/ZnS excited with a 405 nm laser with exposure to air. b) Time resolved photoluminescence transients of InZnN, InZnN/ZnS, InZnN/GaN, and InZnN/GaN/ZnS. c) Photoluminescence decay lifetimes obtained by fitting the transients in (b) with square, circle, and triangle representing τ_1, τ_2, and τ_3, respectively. d) PL stability study of InZnN, InZnN/ZnS, InZnN/GaN, and InZnN/GaN/ZnS nanocrystals in cyclohexane under 405 nm excitation exposed to air.

with the potential for producing unexpected related structures such as the half-Heusler compounds mentioned earlier.

Proof-of-concept devices were prepared to demonstrate the potential of the NCs for application in electroluminescent (EL) devices. The PL spectrum of InZn$_2$N NCs (washed and redispersed in octane to enable device fabrication), along with the EL of a ITO/PEDOT:PSS/InZn$_2$N/Al QDLED under a bias of

−8 V, is shown in **Figure 5**a. Inset to Figure 5a is an image of the QDLED in operation, with the device schematic and a typical J–V scan shown in Figure S15, Supporting Information. EL spectra measured as a function of bias voltage are shown in the inset of Figure 5b, which also shows the corresponding current density and integrated electroluminescence intensity. The turn on voltage for EL is observed at ≈2 V, consistent with the barrier
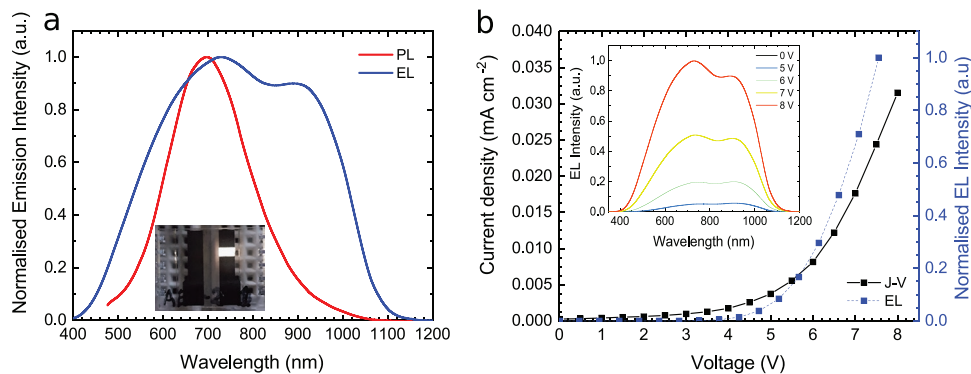

Figure 5. a) Smoothed PL spectrum of InZn$_2$N NCs in octane after washing in ethanol and the EL spectrum of a QDLED, at a bias of 8 V, fabricated using them. Inset to (a) is an image of the QDLED at 7 V. b) Current density (left axis) versus voltage for the QDLED swept obtained using a sweep rate of 0.1 V s^{-1} (J–V, squares/solid line), and integrated electroluminescence (right axis) versus voltage (EL, squares/dotted line). Inset to (b): example spectra used for calculation of the integrated electroluminescence.

**ADVANCED
SCIENCE NEWS**

www.advancedsciencenews.com

**ADVANCED
OPTICAL
MATERIALS**

www.advopticalmat.de

height illustrated for holes in the inset of Figure S15, Supporting Information. Two peaks are clearly visible in the broad EL spectrum with the higher energy peaking at a similar wavelength to the PL. The second lower energy peak ($\approx$950 nm) corresponds to either preferential emission from narrow bandgap NCs (with a lower injection barrier) as illustrated by this peak dominating the lower bias EL spectra, or from the recombination of electrons in the NCs directly with holes in the PEDOT:PSS at the interface. Further device studies and engineering, beyond the scope of this proof-of-principle work, to improve performance characteristics (including turn on voltage) would be expected by the inclusion of an appropriate electron transporting and hole blocking layer between the QDs and aluminum, which would reduce leakage current and improve charge balance. Likewise, increases in device efficiency would also be expected; the EQE of the QDLED device was estimated using an optical power meter as 10^{-3}%.

3. Conclusions

In conclusion, we have shown the synthesis of doped luminescent colloidal nitride NCs, with emission profiles tunable across the visible spectral region into the NIR. Detailed optical and structural characterization is presented with NC PL QY values of up to 30% being achieved. The NCs, were relatively air-sensitive but could be stabilized by the addition of a GaN and ZnS shell. This resulted in a material with much-enhanced durability and emission characteristics, which is desirable for practical applications, such as a colloidal nitride-based QDLED. These NCs have the potential to replace heavy metal-containing quantum dots and are of relevance in the display and potentially bio-imaging industries.

4. Experimental Section

Chemicals: All chemicals were used as purchased from Sigma-Aldrich and used as received unless stated. Indium (III) iodide anhydrous 99.999% (Alpha Aesar), gallium (III) iodide anhydrous 99.999% (Alpha Aesar), octadecene 90%, sodium amide (Acros 99%), zinc stearate 99%, zinc acetate dihydrate 99% (Fisher Scientific), oleic acid reagent grade, zinc diethyldithiocarbamate 97%, 1-hexadecanethiol 95%, cyclohexane 99.5% (anhydrous), and ethanol (anhydrous). The cyclohexane and ethanol were further degassed by bubbling N_2 gas through the solution for 30 min. Octadecene was placed under vacuum at 100 °C for 60 min and then cooled and kept under N_2 gas. 0.12 M Zinc oleate in ODE was prepared as described previously.[31]

Synthesis of InZnN Nanocrystals: In a typical In:Zn 1:1 synthesis, indium (III) iodide (300 mg, 0.6 mmol) was left stirring with hexadecanethiol (308 µL, 1 mmol) in a glovebox to produce a clear solution. This solution was then added to a three-neck vessel with sodium amide (500 mg, 12.8 mmol), zinc stearate (379 mg, 0.6 mmol), and octadecene (20 mL) in a glove box and sealed with septums. The system was transferred to a Schlenk line under positive N_2 pressure and the atmosphere purged under N_2 for a further 30 min. The system was then heated to 240 °C under vigorous stirring. Aliquots were taken at regular intervals. The solution was cleaned in an inert atmosphere by adding 1:1 ratio of cyclohexane and NC solution then centrifuged at 4000 rpm for 5 min to remove by-products such as NaI. The clear nanocrystal solution was further cleaned using ethanol as a non-solvent and centrifuged at 4000 rpm for 5 min and the supernatant discarded. The remaining

nanocrystals were redispersed in small amounts cyclohexane. For the InN, $InZn_{0.5}N$, and $InZn_2N$ reactions, 0 mg, 180 mg (0.3 mmol), and 758 mg (1.2 mmol) respectively of zinc stearate were used.

Synthesis of ZnS Shelled Nanocrystals: In a typical In:Zn 1:1 synthesis and shelling, indium (III) iodide (300 mg, 0.6 mmol) was left stirring with hexadecanethiol (308 µL, 1 mmol) in a glovebox to produce clear solution. This solution was then added to a three-neck vessel with sodium amide (500 mg, 12.8 mmol), zinc stearate (379 mg, 0.6 mmol), and octadecene (20 mL) in a glove box and sealed. The system was transferred to a Schlenk line under positive N_2 pressure and left to degas under N_2 for a further 30 min. The system was then heated to 240 °C and the nanocrystals allowed to grow for 30 min. The solution was allowed to cool to room temperature and transferred to a sealed N_2-filled centrifuge tube. The solution was centrifuged at 4000 rpm for 5 min. Half of the clear solution was then transferred into a new 50 mL 3-neck vessel under N_2 with 0.5 g degassed zinc diethyldithiocarbamate and raised to 175 °C for 30 min. The nanocrystal solution was cleaned as described above.

Synthesis of GaN Shelled Nanocrystals: In a typical synthesis, InZnN nanocrystals were made as above. The solution was allowed to cool to room temperature and transferred to a sealed N_2-filled centrifuge tube. The solution was centrifuged at 4000 rpm for 5 min. Half of the clear solution was then transferred into a new 50 mL 3-neck round vessel under N_2 and 135 mg (0.3 mmol) gallium iodide which had been pre-dissolved in hexadecanethiol 154 µL (0.5 mmol) was then added. This solution was raised to 220 °C for 40 min. The nanocrystal solution was cleaned as described above.

Synthesis of ZnS shelled InZnN/GaN Nanocrystals: In a typical synthesis, InZnN/GaN nanocrystals were made as above. The solution was allowed to cool to room temperature. 7.5 mL of the solution was then transferred into a new 50 mL 3-neck vessel under N_2 with 0.375 mg zinc diethyldithiocarbamate and raised to 175 °C for 30 min. The nanocrystal solution was cleaned as described above.

QDLED Devices: QDLED devices were fabricated on patterned ITO on glass substrates from Ossila Ltd., with an ITO thickness of 100 nm. After cleaning, 100 µL of PEDOT:PSS was spin-coated onto the substrates at 5000 rpm to produce a layer 40 nm thick. In a nitrogen glovebox, $InZn_2N$ QDs were washed by centrifugation in ethanol, then re-dispersed in Octane at 10 mg mL^{-1}. 50 µL of the QD solution was then spin-coated at 2000 rpm producing a layer of QDs approximately 200 nm thick. Without removal from the glovebox, 200 nm of aluminum was then thermally evaporated using a shadow mask to form the cathode. This device architecture and the energy levels of each layer are illustrated in the inset of Figure S15, Supporting Information. The active area was encapsulated using UV-cured epoxy and a glass cover slip to prevent degradation in air during measurement.

Characterization: Absorption spectroscopy was conducted using a Hitachi 4100 absorption spectrometer. PL studies were undertaken using 405 nm laser diode excitation with emission detected using an Ocean Optics QE 4100 spectrometer with 450 nm long pass filter. PL stability studies were carried out using 10 mm quartz cuvette with 2.5 mL cyclohexane.

For PL QY measurements a Newport 3.3-in. integrating sphere was utilized and the resultant PL flux measured with a calibrated Newport 818-SL silicon photodetector or collected for analysis using an Ocean optics QE 4100 spectrometer. The absolute QY were calculated using the method reported previously.[32] PL time decays were recorded using a time correlated single photon counting (TCSPC) system previously reported.[33] This employed a mode-locked Ti:sapphire laser (Mai-Tai HP, spectra physics) to produce 100 fs pulses at a repetition rate of 80 MHz and 840 nm wavelength. The repetition rate was reduced to 4 MHZ or 1 MHz by an acousto-optic pulse picker (APE select) and the initial wavelength halved (to 420 nm) via second harmonic generation (APE harmonic generator). These pulses were used to excite the samples with an average power of 1–2 mW. The PL emission of the samples was collected and focused into a monochromator (Spex 1870c) and detected at the PL peak (or selected wavelength within the PL spectra of each sample) by a multi-channel plate (Hamamatsu R3809U-50). The time correlation of the detected photons was performed

**ADVANCED
SCIENCE NEWS**

www.advancedsciencenews.com

**ADVANCED
OPTICAL
MATERIALS**

www.advopticalmat.de

with the use of a PC electronic card from Edinburgh Instruments. All these measurements were performed at room temperature. The instrument response factor of the TCSPC system is shown in Figure S16, Supporting Information.

For TEM, cleaned samples were drop cast on to Agar Scientific ultra-thin holey carbon supported on a Cu 400 mesh grid and was conducted on JEOL 2100 running at 80 kV or for 300 kV investigations an FEI Technai F30. EDS was taken on Oxford Instruments EDS detector. High angle annular dark field (HAADF) STEM imaging was conducted using an FEI Titan G2 ChemiSTEM running at 200 kV with an electron beam current of 80 pA. STEM-EDS maps were recorded using SuperX EDS system of the Titan and using the Bruker esprit software. Air exposure of the samples was minimized using argon baths. Simulated diffraction patterns were generated using CrystalMaker and SingleCrystal. Powder XRD was conducted on a Cu-Kα PANalytical X'Pert Powder diffractometer or a Bruker D8 Advance theta-theta diffractometer (435 mm diameter) with a Mbraun PSD in Bragg–Brentano geometry employing a Copper Line Focus X-ray tube with Ni K_β absorber (0.02 mm; K_β = 1.392250 Å) K_α radiation ($K_{\alpha 1}$ = 1.540598 Å, $K_{\alpha 2}$ = 1.544426 Å, K_α ratio 0.5, K_α ave = 1.541874 Å) 2° primary Soller slits, 0.2 mm incident slit, and 2° receiving Soller slits.

Samples for XPS required a ligand exchange to the shorter chain tributylphosphine to help prevent excess charging during the measurements, using methods similar to those reported.[31,34] These samples were prepared by adding excess tributylphosphine to a cleaned NC solution and left overnight under nitrogen. The samples were cleaned and redispersed with excess ethanol and cyclohexane, respectively as above and stored under nitrogen.

The samples were rapidly drop-cast onto 40 nm Au-coated glass substrates in nitrogen glovebox, and inserted into the vacuum system of the spectrometer via a nitrogen filled glovebox ante-chamber.

Lab-based XPS was taken using Kratos Axis Ultra with Al Kα X-ray source. Depth-profiling SR-XPS experiments were carried out on the CNR beamline BACH at the Elettra synchrotron facility in Trieste, Italy, using a Scienta R3000 electron energy analyzer. SR-XPS spectra were recorded at normal emission geometry at an angle of 60° between incident X-rays and analyzed photoelectrons, using light linearly polarized in the scattering plane. Excitation energies ($h\nu$) were chosen according to the Einstein equation (KE = $h\nu$ − BE) to create photoelectron spectra of fixed kinetic energy sets from various elemental core levels of known binding energies (BE). Since the inelastic mean free path (λ) of generated photoelectrons was KE dependent, studying such fixed KE sets fixed the sampling depth (defined as 3λ) from which they originate. To carry out a depth-profile analysis, photon energies were chosen such that when measuring various elemental peaks, sets of data with constant photoelectron KE of 225, 550, and 800 eV were obtained. These KE sets were carefully chosen such that there is no interference from major Auger peaks from any of the elements present in the samples. The sampling depth was estimated assuming a planar geometry using the TPP parameters, as described in reference.[35] Binding energies were calibrated to Au 4f$_{7/2}$ 84.0 eV and signal intensities were corrected for the incident photon flux and for X-ray photoionization cross sections.[36] A correction procedure for experimental factors such as beamline flux and electron analyzer response was carried out in IGOR Pro (Wavemetrics) data evaluation software and subsequent peak fitting and analysis was done in CASA software.

Cyclic voltammetry was performed on a BASI Epsilon electrochemical workstation with a 3-electrode cell, Ag/AgNO$_3$ as a reference electrode, platinum wire as a counter electrode, and platinum disc (diameter = 3 mm). Thin films of NCs were drop cast from cyclohexane on an inverted platinum disc working electrode inside a glovebox. The cyclohexane was allowed to evaporate and the electrochemical cell assembled inside a glovebox with prepared 0.1 M acetonitrile solution (anhydrous) of tetrabutylammonium hexafluorophosphate as a supporting electrolyte. Onset potentials were given relative to a ferrocene Fc/Fc+ internal standard redox couple which was taken to be 5.39 eV below vacuum,[37] using the formula: $E_{(HOMO)} = -(E_{(onset\ [O]\ vs\ Fc/Fc+)} + 5.39)$ eV and $E_{(LUMO)} = -(E_{(onset\ [R]\ vs\ Fc/Fc+)} + 5.39)$ eV.

For LED device characterization, PL and EL spectra were recorded using a Horiba iHR320 and Syncerity cooled CCD. All spectra shown have been corrected for the system's spectral response. A high-density monochromator grating was used, requiring multiple scans of the CCD to construct the spectra, as a result smoothing of the data was performed to eliminate artefacts from the CCD boundaries (Figure S15a, Supporting Information).

Electrical measurements were performed on a Kiethley 2636b source measurement unit. Current measurements performed concurrently with EL measurements were averages of the current measured during the spectrum scan.

Supporting Information

Supporting Information is available from the Wiley Online Library or from the author.

Conflict of Interest

The authors declare no conflict of interest.

Keywords

[1] Y. Yin, A. P. Alivisatos, *Nature* **2005**, *437*, 664.

[2] a) Y. Shirasaki, G. J. Supran, M. G. Bawendi, V. Bulović, *Nat. Photonics* **2013**, *7*, 13; b) G. Konstantatos, E. H. Sargent, *Nat. Nanotechnol.* **2010**, *5*, 391; c) R. Saran, R. J. Curry, *Nat. Photonics* **2016**, *10*, 81.

[3] a) T. Schroeder, *Nature* **2008**, *453*, 345; b) X. Gao, X. Cui, R. M. Levenson, L. W. K. Chung, S. Nie, *Nat. Biotechnol.* **2004**, *22*, 969.

[4] a) B. Mazumder, A. L. Hector, *J. Mater. Chem.* **2009**, *19*, 4673; b) S. Nakamura, T. Mukai, M. Senoh, *Appl. Phys. Lett.* **1994**, *64*, 1687.

[5] A. G. Bhuiyan, A. Hashimoto, A. Yamamoto, *J. Appl. Phys.* **2003**, *94*, 2779.

[6] a) H. Amano, I. Akasaki, T. Kozawa, K. Hiramatsu, N. Sawaki, K. Ikeda, Y. Ishii, *J. Lumin.* **1988**, *40-41*, 121; b) I. Akasaki, H. Amano, *Jpn. J. Appl. Phys.* **2006**, *45*, 9001; c) C. J. Neufeld, N. G. Toledo, S. C. Cruz, M. Iza, S. P. DenBaars, U. K. Mishra, *Appl. Phys. Lett.* **2008**, *93*, 143502.

[7] J. Choi, E. G. Gillan, *J. Mater. Chem.* **2006**, *16*, 3774.

[8] a) P. Reiss, M. Carrière, C. Lincheneau, L. Vaure, S. Tamang, *Chem. Rev.* **2016**, *116*, 10731; b) M. V. Kovalenko, L. Manna, A. Cabot, Z. Hens, D. V. Talapin, C. R. Kagan, V. I. Klimov, A. L. Rogach, P. Reiss, D. J. Milliron, P. Guyot-Sionnnest, G. Konstantatos, W. J. Parak, T. Hyeon, B. A. Korgel, C. B. Murray, W. Heiss, *ACS Nano* **2015**, *9*, 1012.

[9] a) P. K. B. Palomaki, E. M. Miller, N. R. Neale, *J. Am. Chem. Soc.* **2013**, *135*, 14142; b) N. S. Karan, Y. Chen, Z. Liu, R. Beaulac, *Chem. Mater.* **2016**, *28*, 5601; c) U. Guler, S. Suslov, A. V. Kildishev, A. Boltasseva, V. M. Shalaev, *Nanophotonics* **2015**, *4*, 269; d) P. N. Taylor, M. A. Schreuder, T. M. Smeeton, A. J. D. Grundy, J. A. Dimmock, S. E. Hooper, J. Heffernan, M. Kauer, *J. Mater. Chem. C* **2014**, *2*, 4379.

[10] a) Z. Liu, R. Beaulac, *Chem. Mater.* **2017**, *29*, 7507; b) Y. C. Choi, H. Kim, C. Lee, J. Son, H. Baik, S. Park, J. Kim, K. S. Jeong, *Chem. Mater.* **2019**, *31*, 5370; c) H. F. Gaiser, R. Popescu, D. Gerthsen, C. Feldmann, *Chem. Commun.* **2020**, *56*, 2312.

[11] a) J. Zhang, D. Zhang, *CrystEngComm* **2010**, *12*, 591; b) U. T. D. Thuy, P. Reiss, N. Q. Liem, *Appl. Phys. Lett.* **2010**, *97*, 193104.

[12] a) B. R. Nag, *Phys. Status Solidi B* **2003**, *237*, R1; b) H. Morkoç, S. N. Mohammad, *Science* **1995**, *267*, 51; c) W. M. Xie, Q. Y. Xie, H. P. Zhu, W. Wang, H. L. Cai, F. M. Zhang, X. S. Wu, *J. Phys. D: Appl. Phys.* **2015**, *48*, 215102.

[13] M. D. Clark, S. K. Kumar, J. S. Owen, E. M. Chan, *Nano Lett.* **2011**, *11*, 1976.

[14] L. Qu, X. Peng, *J. Am. Chem. Soc.* **2002**, *124*, 2049.

[15] R. Ahumada-Lazo, S. M. Fairclough, S. J. O. Hardman, P. N. Taylor, M. Green, S. J. Haigh, R. Saran, R. J. Curry, D. J. Binks, *ACS Appl. Nano Mater.* **2019**, *2*, 7214.

[16] C. G. Van de Walle, J. Neugebauer, *Nature* **2003**, *423*, 626.

[17] S.-H. Yoo, A. Walsh, D. O. Scanlon, A. Soon, *RSC Adv.* **2014**, *4*, 3306.

[18] a) M. Protière, P. Reiss, *Small* **2007**, *3*, 399; b) X. Zhong, Y. Feng, W. Knoll, M. Han, *J. Am. Chem. Soc.* **2003**, *125*, 13559; c) R. E. Bailey, S. Nie, *J. Am. Chem. Soc.* **2003**, *125*, 7100.

[19] a) J. Wang, G. Tang, X. S. Wu, M. Gu, *Solid State Commun.* **2012**, *152*, 1168; b) B. Zhang, H. Song, X. Xu, J. Liu, J. Wang, X. Liu, S. Yang, Q. Zhu, Z. Wang, *Nanotechnology* **2011**, *22*, 235603; c) H. Song, A. Yang, R. Zhang, Y. Guo, H. Wei, G. Zheng, S. Yang, X. Liu, Q. Zhu, Z. Wang, *Cryst. Growth Des.* **2009**, *9*, 3292.

[20] R. Juza, H. Hahn, *Z. Anorg. Allg. Chem.* **1938**, *239*, 282.

[21] M. Futsuhara, K. Yoshioka, O. Takai, M. Androulidaki, M. Ruzinsky, V. Saly, P. Prokien, Z. Viskadourakis, K. Tsagaraki, E. Aperathitis, *Thin Solid Films* **1998**, *322*, 274.

[22] a) M. Mapa, K. Sivaranjani, D. S. Bhange, B. Saha, P. Chakraborty, A. K. Viswanath, C. S. Gopinath, *Chem. Mater.* **2010**, *22*, 565; b) A. Miyaake, Y. Masubuchi, T. Takeda, S. Kikkawa, *Mater. Res. Bull.* **2010**, *45*, 505; c) H. Gao, X. Zhang, Y. Zhao, B. Yan, *AIP Adv.* **2017**, *7*, 025111.

[23] K. A. Mkhoyan, J. Silcox, *Appl. Phys. Lett.* **2003**, *82*, 859.

[24] a) C. T. Smith, M. A. Leontiadou, P. C. J. Clark, C. Lydon, N. Savjani, B. F. Spencer, W. R. Flavell, P. O'Brien, D. J. Binks, *J. Phys. Chem. C* **2017**, *121*, 2099; b) P. Huang, J. Shi, P. Wang, M. Zhang, Y. Ding, M. Wu, J. Lu, X. Wang, *J. Mater. Chem. A* **2016**, *4*, 17412.

[25] a) K. R. Reyes-Gil, E. A. Reyes-García, D. Raftery, *J. Phys. Chem. C* **2007**, *111*, 14579; b) L. Wang, Q. Shen, D. Zhao, J. Lu, W. Liu, J. Zhang, K. Bao, Q. Zhou, *J. Cryst. Growth* **2017**, *471*, 62; c) E. Lee, T. Kim, A. Benayad, J. Hur, G.-S. Park, S. Jeon, *Sci. Rep.* **2016**, *6*, 23940.

[26] K. S. A. Butcher, A. J. Fernandes, P. P. T. Chen, M. Wintrebert-Fouquet, H. Timmers, S. K. Shrestha, H. Hirshy, R. M. Perks, B. F. Usher, *J. Appl. Phys.* **2007**, *101*, 123702.

[27] D. G. Castner, K. Hinds, D. W. Grainger, *Langmuir* **1996**, *12*, 5083.

[28] X. Zhang, L. Yu, A. Zakutayev, A. Zunger, *Adv. Funct. Mater.* **2012**, *22*, 1425.

[29] M. Oda, J. Tsukamoto, A. Hasegawa, N. Iwami, K. Nishiura, I. Hagiwara, N. Ando, H. Horiuchi, T. Tani, *J. Lumin.* **2007**, *122-123*, 762.

[30] K. S. A. Butcher, H. Hirshy, R. M. Perks, M. Wintrebert-Fouquet, P. P.-T. Chen, *Phys. Status Solidi A* **2006**, *203*, 66.

[31] S. M. Fairclough, E. J. Tyrrell, D. M. Graham, P. J. B. Lunt, S. J. O. Hardman, A. Pietzsch, F. Hennies, J. Moghal, W. R. Flavell, A. A. R. Watt, J. M. Smith, *J. Phys. Chem. C* **2012**, *116*, 26898.

[32] J. C. de Mello, H. F. Wittmann, R. H. Friend, *Adv. Mater.* **1997**, *9*, 230.

[33] D. Espinobarro-Velazquez, M. A. Leontiadou, R. C. Page, M. Califano, P. O'Brien, D. J. Binks, *ChemPhysChem* **2015**, *16*, 1239.

[34] P. C. J. Clark, H. Radtke, A. Pengpad, A. I. Williamson, B. F. Spencer, S. J. O. Hardman, M. A. Leontiadou, D. C. J. Neo, S. M. Fairclough, A. A. R. Watt, I. Pis, S. Nappini, F. Bondino, E. Magnano, K. Handrup, K. Schulte, M. G. Silly, F. Sirotti, W. R. Flavell, *Nanoscale* **2017**, *9*, 6056.

[35] S. Tanuma, C. J. Powell, D. R. Penn, *Surf. Interface Anal.* **2003**, *35*, 268.

[36] J.-J. Yeh, *Atomic Calculation of Photoionization Cross-Sections and Asymmetry Parameters*, Gordon and Breach, Langhorne, PA **1993**.

[37] C. M. Cardona, W. Li, A. E. Kaifer, D. Stockdale, G. C. Bazan, *Adv. Mater.* **2011**, *23*, 2367.

2000604 (9 of 9)